Supplementary Information

Unleashing the Power of Directed Electron Transfer: Unraveling the Potential of $\{PV_4\}_2$ in Heterogeneous Photocatalysis

Xin Su, [a] *Yuzan He,* [a] *Kunhong Li,* [a] *Miao Wang,* [a] *Wei Tang,* [a] *Shihao Zhang,* [a] *Pengtao Ma,* [a] *Jingyang Ni,** [a] *and Jingping Wang** [a]
Corresponding Authors: jyniu@henu.edu.cn (J.Y. Niu); jpwang@henu.edu.cn (J.P. Wang)

Henan Key Laboratory of Polyoxometalate Chemistry, College of Chemistry and Molecular Sciences, Henan University, Kaifeng, Henan, 475004 (P. R. China).

Section 1. Experimental section 2
Section 2. Crystallographic data for $\{PV_4\}_2$ 4
Section 3. Photocatalysis experiment and characterization. 6
Section 4. DFT calculation 14
References 17

Section 1. Experimental section

1.1. Materials and Methods

All chemicals were purchased from Aladdin without any pre-treatment. The purity of Ar and CO_2 was 99.999%. The purity of all solvents was analytically pure. Fourier transform infrared (FTIR) spectroscopic was obtained using KBr pellets on a Perkin-Elmer Spectrum Two spectrophotometer. Powder X-ray diffraction (PXRD) patterns were recorded using a Bruker D8 ADVANCE diffractometer with Cu Kα radiation (λ=1.54056 Å). Thermogravimetric (TG) analysis was performed using a Perkin Elmer TGA7 instrument. X-ray photoelectron spectroscopy (XPS) measurement was conducted with an Axis Ultra X-ray photoelectron spectroscope equipped with monochromatic Al Kα (1486.7 eV) radiation. UV-visible diffuse reflectivity spectroscopy was performed on a UV-2600 instrument. Steady-state photoluminescence (PL) and time-resolved photoluminescence (TRPL) spectroscopy were recorded using an Edinburgh FLS980 spectrometer. Scanning electron microscopy (SEM) images were acquired on a ZEISS Gemini 300 scanning electron microscope. CO_2 gas adsorption was tested by Microtrac Belsorp-HP at 25°C. Crystal data was collected using a Bruker D8 VENTURE PHOTON II diffractometer with a graphite-monochromate Mo Kα (λ = 0.71073 Å) radiation source in a 150 K cooled nitrogen stream. The SHELXT structure solver was used for structure determination, and the SHELXL refinement package in Olex 2 was used for full matrix least squares refinement on F^2 data. Elemental analyses (C, H, N) were conducted using Elementary Vario MICRO analyzer. Quantitative analyses of all elements were performed using a PerkinElmer Optima 2100 DV inductively coupled plasma (ICP) optical-emission spectrometer. Electrochemical measurements were conducted using a CHI 760E electrochemical workstation. The products of Isotope-labeled experiments were analyzed with Agilent Gas chromatography-mass spectrometry (GC-9890Plus-5977C GC/MSD). Capillary column (Plot) was used for gas chromatography. The ion source temperature of 5977C GC/MSD was 230°C. The ionization energy was 70 eV. The collection mode of mass spectrum was Select ion monitoring mode (SIM).

Fig. S1. The synthetic route of $\{PV_4\}_2$

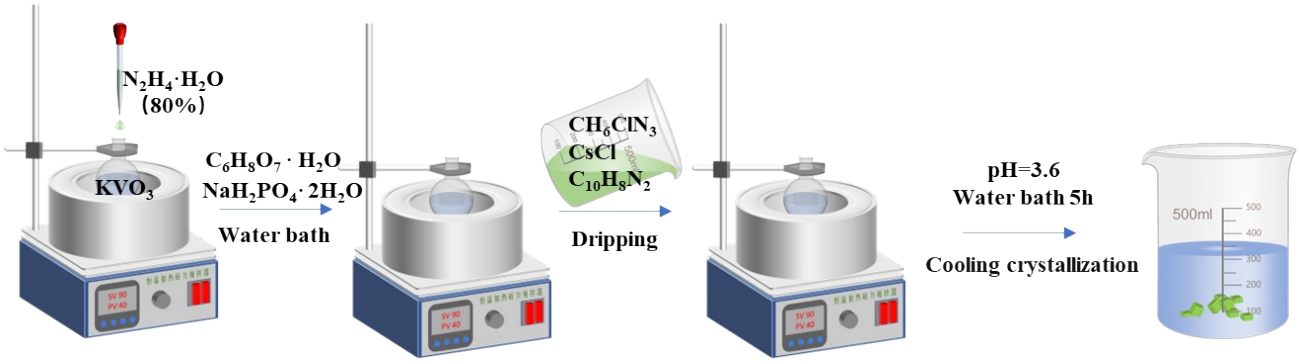

1.2 Photocatalytic reaction

The photocatalytic CO_2 reduction reaction was conducted in a 50 mL closed quartz reactor (Fig. S2). During the experiment, the as-prepared catalyst ($\{PV_4\}_2$, 10 mg), photosensitizer ($[Ru(bpy)_3Cl_2 \cdot 6H_2O$, 0.01 mmol), acetonitrile (15 mL), and triethanolamine (TEOA, 0.5 mL) were dispersed in the quartz reactor. High-purity CO_2 gas was pumped into the reactor for 30 minutes. During the reaction, the products were injected into the gas chromatography (GC-9890Plus) through the injection needle for subsequent quantitative analysis. Reaction rate(R_s), Electron consumption rate (R_e), selectivity (S) and Apparent Quantum Yield (AQY) of photocatalytic CO_2 reduction reaction were calculated by the following equations (eq.1-4):

$$R_s = \frac{n_s}{mt} \qquad \text{(eq. 1)}$$

$$R_e = R_{co}K_1 + R_{CH4}K_2 \qquad \text{(eq. 2)}$$

$$S = \frac{R_s}{R_e} = \frac{R_1}{R_{CO}K_1 + R_{CH4}K_2} \qquad \text{(eq. 3)}$$

$$AQY = \frac{2.4 \times 10^8 v}{IA\lambda} \times 100\% \qquad \text{(eq. 4)}$$

where *Rs* is the reaction rate ($\mu mol \cdot h^{-1} \cdot g^{-1}$), *t* is the reaction time (h), *m* is the catalyst content (g), n_s is the yield of reduced products (μmol). R_e is the electron consumption rate ($\mu mol \cdot h^{-1} \cdot g^{-1}$), R_{co}, R_{CH4} are the reaction rate of CO and CH_4 ($\mu mol \cdot h^{-1} \cdot g^{-1}$), K_1, K_2 are the number of electrons transferred by different products (K_1=2; K_2=8). *S* is the selectivity of the target product, *Rs* is the reaction rate of the target product, R_e is the electron consumption rate of the target product. v is the reaction rate ($mol \cdot s^{-1}$), *I* is the optical power density ($W \cdot m^{-2}$), *A* is illumination area (m^2), λ *is* incident wavelength (nm).

The calculation formula of the band gap energy

$$(\alpha h\nu)^{1/m} = B(h\nu - E_g) \qquad \text{(eq. 5)}$$

α is the absorption coefficient, B is the constant, $h\nu$ is the photon energy, h is the Planck constant (4.13×10^{-15} eV·s) , ν is the incident photon frequency, E_g is band gap energ.

1.2 Electrochemical measurements

All electrochemical measurements were performed in CHI 760e, the sample modified FTO glass (1 cm×2 cm), Ag/AgCl electrode and Pt sheet electrode were used as the working electrode, reference electrode and counter electrode. The electrolyte solution was 0.5 mol·L^{-1} $KHCO_3$ aqueous solution. The Mott-Schottky plots were measured over an alternating current (AC) frequency of 1,000 Hz, 2000 Hz and 3000 Hz at -0.6V vs. NHE. The LSV tests were performed under visible light conditions, and the required gases (CO_2 and Ar) were pumped into the electrolyte solution for 30min before test.

Fig. S2. The picture of photocatalytic reaction device

Synthesis of sample modified FTO glass.

The as-synthesized crystals 2 mg were grinded to powder and then dispersed in 2 mL of solvent (1900 μL EtOH and 100 μL 0.5% Nafion) by ultrasonication to form a homogeneous ink. Subsequently, 400 μL of the ink was covered onto FTO glass and dried in room temperature for LSV or Mott–Schottky measurements.

Section 2. Crystallographic data for $\{PV_4\}_2$

The Crystallographic data for $\{PV_4\}_2$ was shown in Table S1, the structure was solved by direct methods with SHELXS–201420 and refined by full–matrix least–squares techniques by the SHELXL–2014 program.

Table S1. Crystal Data and Structure Refinements for $C_{66}H_{157}CsN_{14}Na_2O_{92}P_2V_8$

	Compound 1
Formula	$C_{66}H_{157}CsN_{14}Na_2O_{92}P_2V_8$
Formula weight	3266.63
Temperature (K)	298

Crystal system	orthorhombic
Space group	*Pban*
a (Å)	21.613 (10)
b (Å)	29.212 (10)
c (Å)	11.966 (4)
V (Å^3)	7555 (5)
Z	2
ρ_{calc} (g/cm^3)	1.098
μ (mm^{-1})	0.803
F (000)	2490.0
Crystal size (mm^3)	0.18 × 0.16 × 0.15
Index ranges	$-25 \leq h \leq 25$
	$-34 \leq k \leq 34$
	$-14 \leq l \leq 14$
Reflections collected	48770
Data/restraints/parameters	6727/6/302
GOF on F^2	0.992
R1, *wR2* [I>=2σ (I)]	*R1* = 0.0491, *wR2* = 0.1285
R1, *wR2* [all data]	*R1* = 0.0902, *wR2* = 0.1526

$R_1 = \sum||F_o|-|F_c||/\sum|F_o|$, $wR_2 = \{\sum[w(F_o^2-F_c^2)^2]/\sum[w(F_o^2)^2]\}^{1/2}$

Table S2. Partial bond length (Å) and bond Angle (°) of $\{PV_4\}_2$.

Bond	Length	Bond	Length	Bond	Length
V1−O1	1.596 (3)	P1−O4	1.537 (3)	V1−O8	2.377 (3)
P1−O2	1.544 (3)	V2−O4	1.975 (3)	V1−O10	2.025 (3)
V1−O2	2.002 (3)	V2−O5	1.610 (3)	V2−O10	2.003 (3)
V1−O3	2.049 (3)	V1−O6	2.004 (3)	V2−O11	2.024 (3)
V2-N2	2.292 (3)	V2-N1	2.135 (3)	P1-O2	1.544 (3)
P1-O4	1.537 (3)	V2-N1	3.546 (3)		
Bond	**Angel**	**Bond**	**Angel**	**Bond**	**Angel**
P1−O2−V1	119.82 (15)	O2−V1−O10	101.0 (3)	O4−V2−O11	162.89 (13)
P1−O4−V2	129.87 (17)	O3−V1−O8	99.5 (3)	O5−V2−N1	93.31 (15)
O4−P1−O2	109.02 (14)	O6−V1−O3	154.1 (3)	O5−V2−N2	165.12 (15)
O1−V1−O2	102.06 (14)	O6−V1−O8	80.0 (3)	O5−V2−O4	101.17 (14)
O1−V1−O3	99.50 (15)	O6−V1−O10	80.4 (3)	O5−V2−O10	104.30 (14)
O1−V1−O6	98.94 (15)	O10−V1−O3	89.3 (3)	O5−V2−O11	95.40 (16)
O1−V1−O8	177.83 (14)	O10−V1−O8	154.8 (3)	O10−V2−N1	162.38 (13)

O1−V1−O10	100.72 (15)	N1−V2−N2	103.5 (3)	O10−V2−N2	90.09 (12)
O2−V1−O3	88.30 (11)	O4−V2−N1	103.4 (3)	O10−V2−O11	89.33 (14)
O2−V1−O6	158.99 (13)	O4−V2−N2	101.7 (4)	O11−V2−N1	88.45 (13)
O2−V1−O8	79.84 (10)	O4−V2−O10	60.4 (4)	O11−V2−N2	80.80 (12)

Table S3. The BVS calculation results of V and P atoms in $\{PV_4\}_2$.

Atom	BVS	Atom	BVS	Atom	BVS
V1	3.97	V2	4.05	P1	4.69

Table S4. The BVS calculation results of O atoms in $\{PV_4\}_2$.

Atom	BVS	Atom	BVS	Atom	BVS
O1	1.66	O5	1.60	O9	1.45
O2	1.71	O6	2.03	O10	1.91
O1W	0.43	O7	1.42	O11	1.83
O3	0.57	O8	1.90	O12	1.43

Section 3. Photocatalysis experiment and characterization.

Table S5. Optimize experimental results.

	Catalyst (mg)	Photosensitizer (mmol)	The yield of CO ($\mu mol\ g^{-1}\ h^{-1}$)	The selectivity of CO
a	5	0.01	3487.1	76.44%
b	8	0.01	5625.4	81.27%
c	10	0.01	9113.9	87.61%
d	12	0.01	1107.2	84.94%
e	10	0.005	2214.5	67.32%
f	10	0.008	4396.1	78.16%
g	10	0.01	9113.9	87.61%
h	10	0.012	1168.5	85.26%

Table S6. Optimize experimental results.

Catalyst ($\{PV_4\}_2$)	The yield of CO ($\mu mol\ g^{-1}\ h^{-1}$)			
	TEOA	Na_2SO_3	H_2O	Triethylamine
10 mg	9113.9	3783.1	743.7	7978.6

Table S7. Reaction rate comparison of recently reported semiconductor photocatalysts for CO_2 reduction.

Bond	photosensitizer	Generation Rate of CO (μmol /g·h)	References
This work	$[Ru(bpy)_3]Cl_2$	9113.9	
SiW_{12}@CdMOF PW_{12}@CdMOF	$[Ru(bpy)_3]Cl_2$	320 271	[1]
SiC-$W_{18}O_{49}$		11.96	[2]
Cu/BiOCl		6.375	[3]
phosphorus/Bi_2MoO_6		18.2	[4]
CNA_X		12.58	[5]
g-C_3N_4	Re(bpy-COOH)	22.44	[6]
ZnS–CdSe@Co/N–C		2.67	[7]
$Na_2[Ru(bpy)_3]_2Mn^{II}{}_3[P_4Mo_6O_{25}(OH)_6]_2 \cdot 20 H_2O$	$[Ru(bpy)_3]Cl_2$	$0.4*10^{-6}$	[8]
NENU-606	$[Ru(bpy)_3]Cl_2$	$2*10^{-6}$	[9]
g-C_3N_4		4.81	[10]
AuPd/3DOM-TiO_2		14.0	[11]
Bi_5O_7Cl		27.15	[12]
ZnO/$ZnWO_4$/g-C_3N_4		13.19	[13]
CoSA-N_x/C	$[Ru(bpy)_3]Cl_2$	10110	[14]
$BaTiO_3$	$[Ru(bpy)_3]Cl_2$	5493	[15]
Fe-soc-MOFs		557300	[16]
$Fe(tmhd)_3$		682	[17]
In_2O_3		630	[18]
Ru-UiO-67	BIH	426.05	[19]
CoP	$[Ru(bpy)_3]Cl_2$	68100	[20]
Co_9S_8	$[Ru(bpy)_3]Cl_2$	35000	[21]

Table. S8. The time-resolved photoluminescence (TRPL) of $\{PV_4\}_2$

The time-resolved photoluminescence (TRPL) spectroscopy of $\{PV_4\}_2$ could be well fitted to the bi-exponential model:

The bi-exponential model of $\{PV_4\}_2$ and PS:

$$I_t = A_1 \exp\left(-\frac{t}{\tau_1}\right) + A_2 \exp\left(-\frac{t}{\tau_2}\right) \qquad \text{(eq. S6)}$$

The formula for the average decay life:

$$\tau_{avg} = \frac{A_1\tau_1^2 + A_2\tau_2^2}{A_1\tau_1 + A_2\tau_2} \qquad \text{(eq. S7)}$$

where I_t is the PL intensity, t is the decay time after absorption, τ_1 and τ_2 are the lifetimes of the short and long decay processes, and A_1 and A_2 are the respective PL amplitudes[22].

Samples	τ_1	A_1	τ_1	A_2	τ_{avg}	R_2
PS/$\{PV_4\}_2$	1.96 μs	693.48	17.91 μs	28.48	6.31 μs	0.9811
PS	1.95 μs	2081.21	14.03 μs	190.76	6.75 μs	0.9928
PS/ V_2O_5	1.86 μs	2100.68	12.70 μs	240.25	6.61 μm	0.9947
$\{PV_4\}_2$	1.16 ns	243.77	5.68 ns	111.24	4.28 ns	0.9896
V_2O_5	1.13 ns	288.31	5.18 ns	135.54	3.89 ns	0.9894

Fig. S3. The coordination mode of each atom in polyanion: (a) 2'2-bipyridine; (b) P atom; (c) Na atom

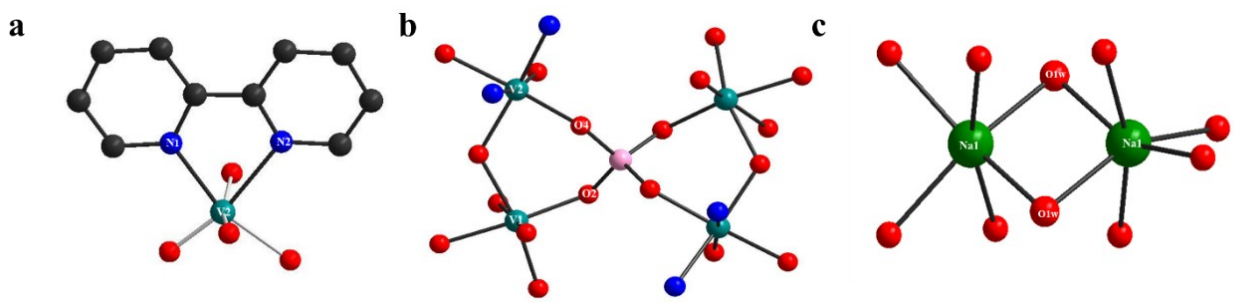

Fig. S4. Actual image (left) and microscope image (right) of $\{PV_4\}_2$.

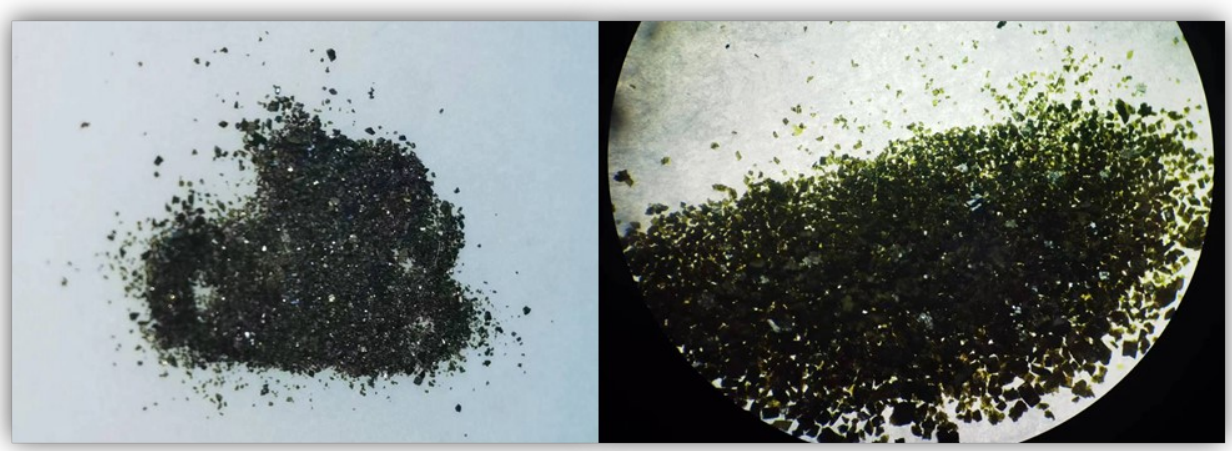

Fig. S5. Scanning electron microscope and elemental mappings picture of $\{PV_4\}_2$.

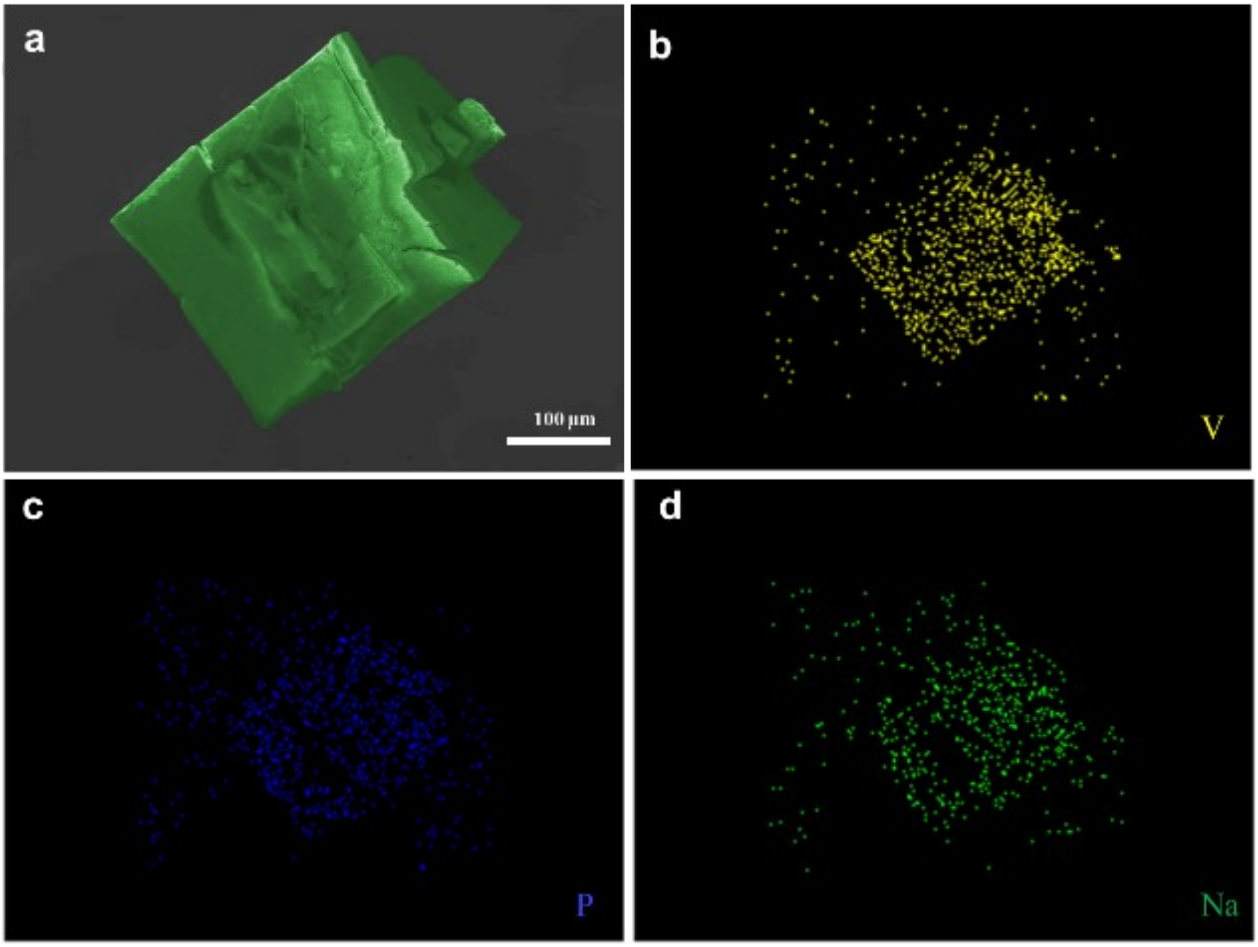

Fig. S6. Thermogravimetric analytical traces of $\{PV_4\}_2$.

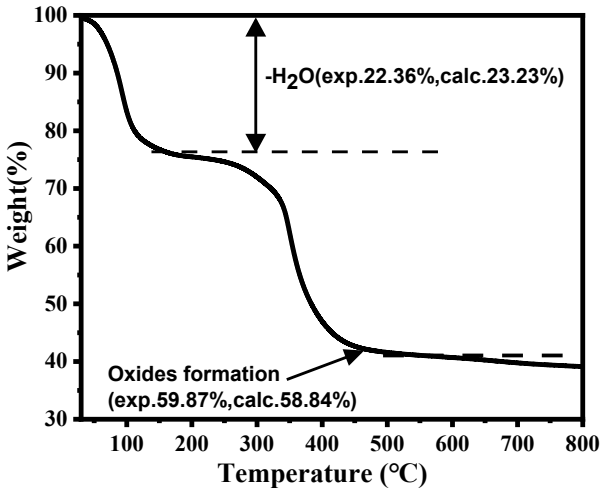

Fig. S7. PXRD and FTIR spectra of $\{PV_4\}_2$ soaked in different solutions.

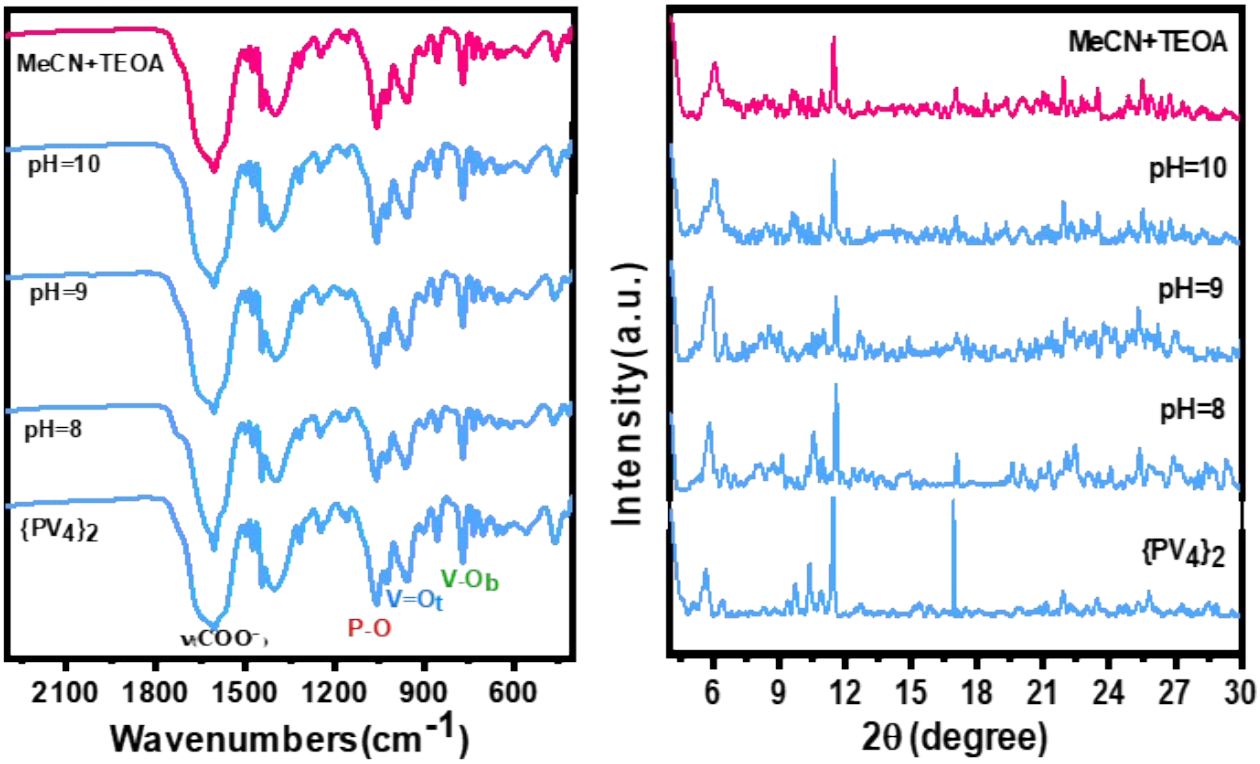

Fig. S8. The standard curves of (a) CO and (b) CH_4; The GC on-line curves of $\{PV_4\}_2$.

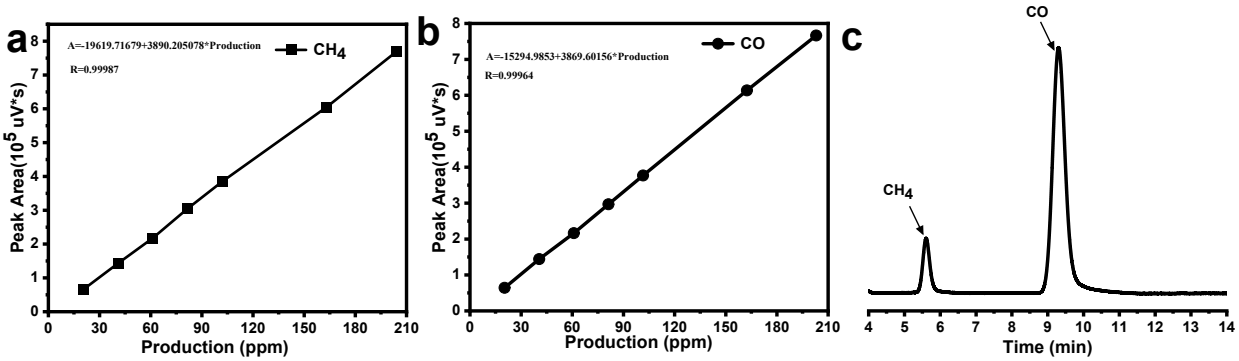

Fig. S9. The apparent quantum efficiency of the $\{PV_4\}_2$ at specific wavelength irradiation.

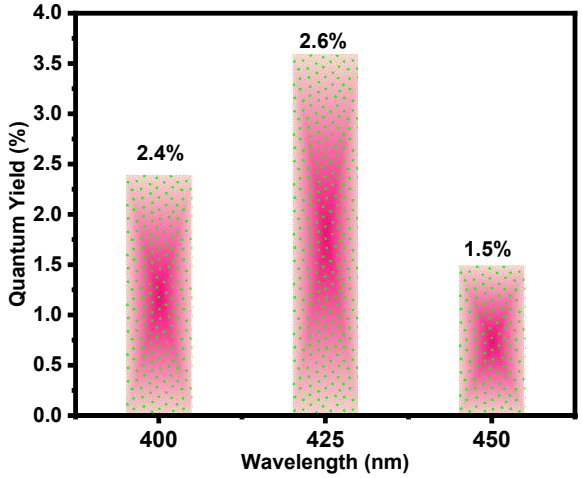

Fig. S10. Time-dependent CO and CH_4 generation process of $\{PV_4\}_2$

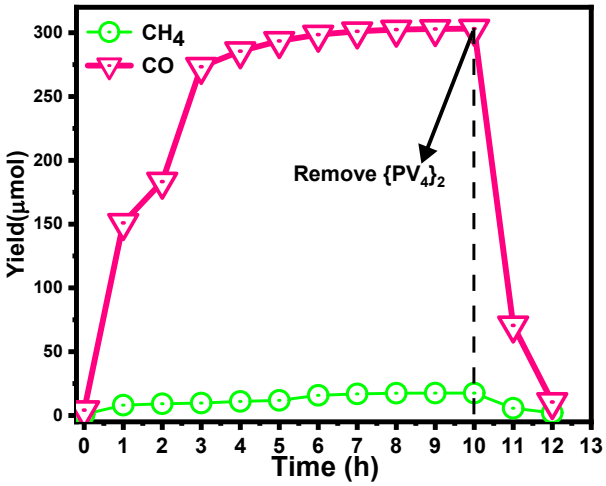

Fig. S11. Isotopic gas product analysis

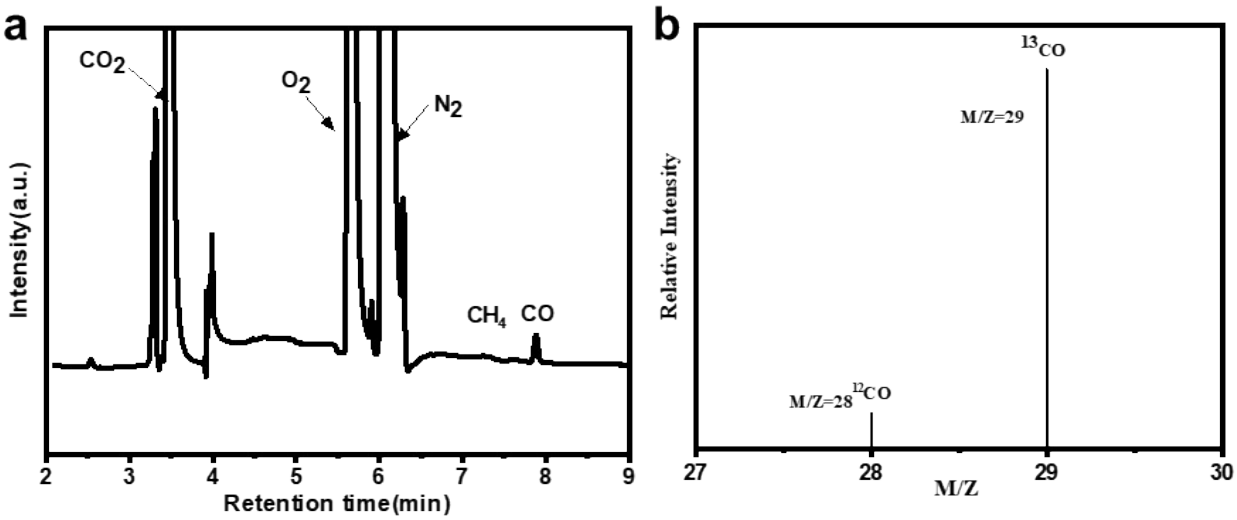

Fig. S12. The FTIR spectra for $\{PV_4\}_2$ before and after reaction.

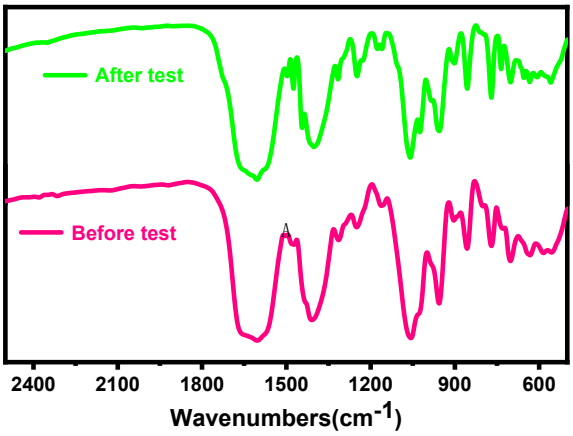

Fig. S13. XPS high-resolution scan of V 2p and P 2p for $\{PV_4\}_2$ before and after reaction.

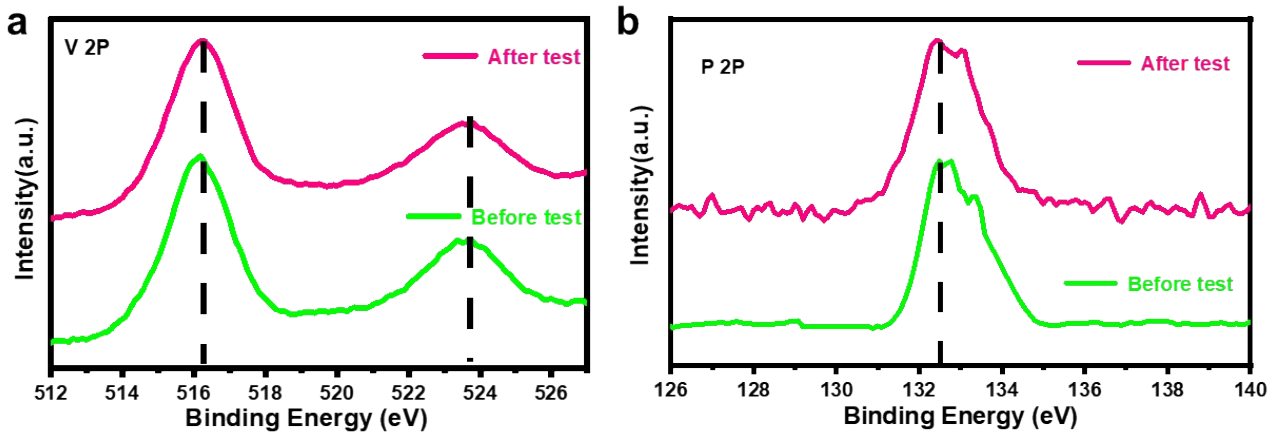

Fig. S14. Time-dependent CO and CH_4 generation process of $\{PV_4\}_2$ in different catalytic systems.

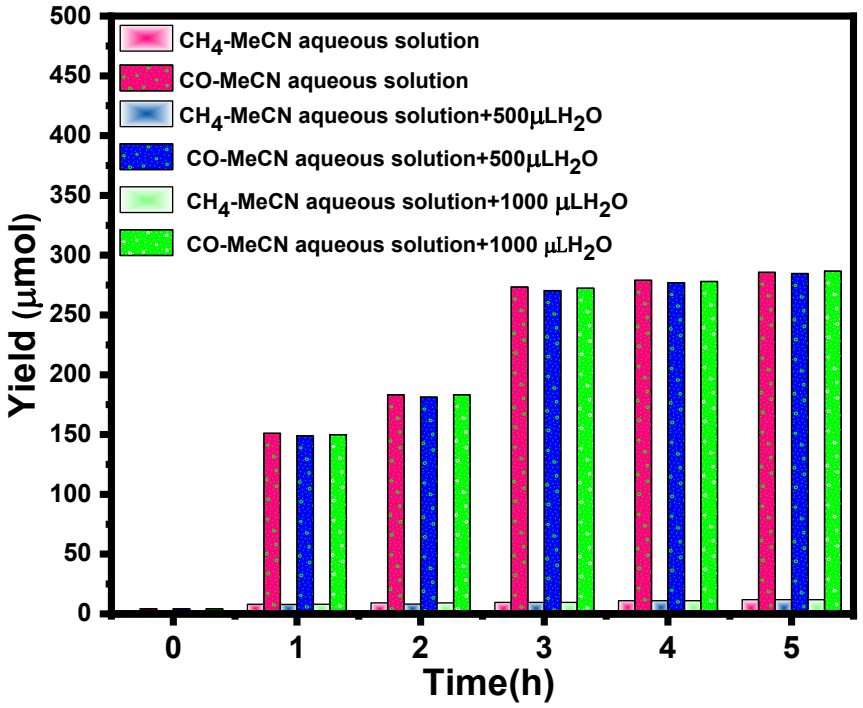

Fig. S15. Time-dependent CO generation process of $\{PV_4\}_2$ and V_2O_5 without $[Ru(bpy)_3]^{2+}$.

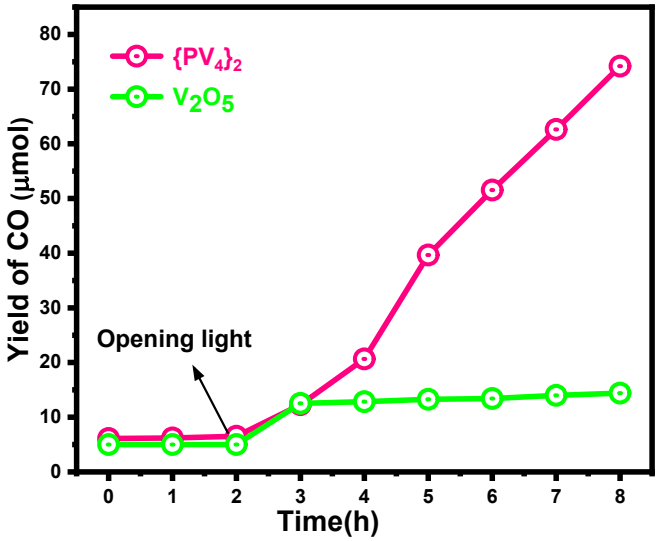

Fig. S16. The transient fluorescence lifetime of $\{PV_4\}_2$ and V_2O_5.

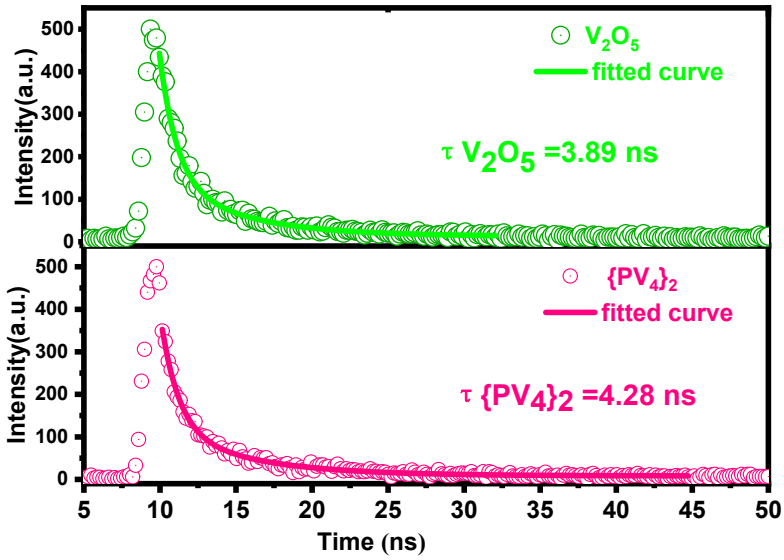

Section 4. DFT calculation

Computational Details and Models

All density functional theory (DFT) calculations were performed using the Gaussian 16 software package[23]. $[Na_2(H_2O)_2P_2V^{IV}_8(cit)_4(bpy)_4O_{16}(H_2O)_4]^{4-}$ pattern was extracted from X-ray crystal

structures and protonated according to the results of the valence bond analysis. Geometries were optimized using the (U)B3LYP functional[24, 25] and Grimme's D3bj dispersion[26, 27] correction with the basis set of 6-31G(d) for all atoms. Vibrational frequencies were calculated for all the stationary points to confirm if each optimized structure was a local minimum on the respective potential energy surface with only one imaginary frequency. Solvation energy corrections were calculated in acetonitrile solvent with the SMD continuum solvation model[27] based on the gas phase optimized geometries. The (U)B3LYP and (U)M06[28] functional with a 6-311+G(d, p) for all atoms were used for single-point energy calculations.

Owing to the presence of d electrons in fully reduced POV, All V atoms in $\{PV_4\}_2$ were tetravalent, each vanadium atom had lone pair electrons. So $\{PV_4\}_2$ molecule exhibited spin multiples. When $\{PV_4\}_2$ was in a singlet state, there might be two forms of singlet opened-shell and singlet closed-shell, because of the arrangement of single electrons. The singlet opened-shell and singlet closed-shell of $\{PV_4\}_2$ was optimized respectively to get the energy level orbital. By comparing the optimized free energy (Table S8) found that the free energy of the opened-shell was lower than that of the closed-shell, indicating that the $\{PV_4\}_2$ existed in the form of the opened-shell (Figure S17). To get the best energy level orbital, other spin multiples of $\{PV_4\}_2$ (nV, n was the number of spin multiples) had been calculated, and all the linear states existing in $\{PV_4\}_2$ after electron acquisition. The free energy profile of spin multiples $\{PV_4\}_2$ radical cross-coupling was shown in Supplementary Table S8. Our computational results showed that the singlet opened shell of $\{PV_4\}_2$ was highly unstable compared with the 9V-N of $\{PV_4\}_2$. Therefore, the spin state of $\{PV_4\}_2$ preferred to be 9V-N. After $\{PV_4\}_2$ had obtained photogenerated electrons, the 2V-D of $\{PV_4\}_2$ was highly unstable compared with 6V-S of $\{PV_4\}_2$, and other spin multiples had higher relative free energies than their corresponding 6V-S. Therefore, when $\{PV_4\}_2$ achieved photogenerated electrons, it became the 6V-S of $\{PV_4\}_2$ (Figure S18).

Table S9. The free energy profile of spin multiples of $\{PV_4\}_2$

linear states	B3LYP free energy (a.u.)	M06 free energy insolution (a.u.)
$1V_{singlet}$ - closed-shell	-15234.709164	-15232.981513
$1V_{singlet}$ - opened-shell	-15234.957777	-15233.19975
$3V_{Triplet}$	-15234.958926	-15233.201096
$5V_{Quintuplet}$	-15234.959484	-15233.201122
$7V_{Septet}$	-15234.959885	-15233.201846
$9V_{Nonet}$	-15234.960221	-15233.202362
$2V_{Doublet}$	-15234.773173	-15233.295304
$4V_{Quartet}$	-15234.774893	-15233.292683
$6V_{Sextet}$	-15234.775429	-15233.29555
$8V_{Octet}$	-15234.774328	-15233.293525
$10V_{Decuplet}$	-15234.774184	-15233.29354

Fig. S17. Optimized structure diagram of singlet opened-shell and singlet closed-shell.

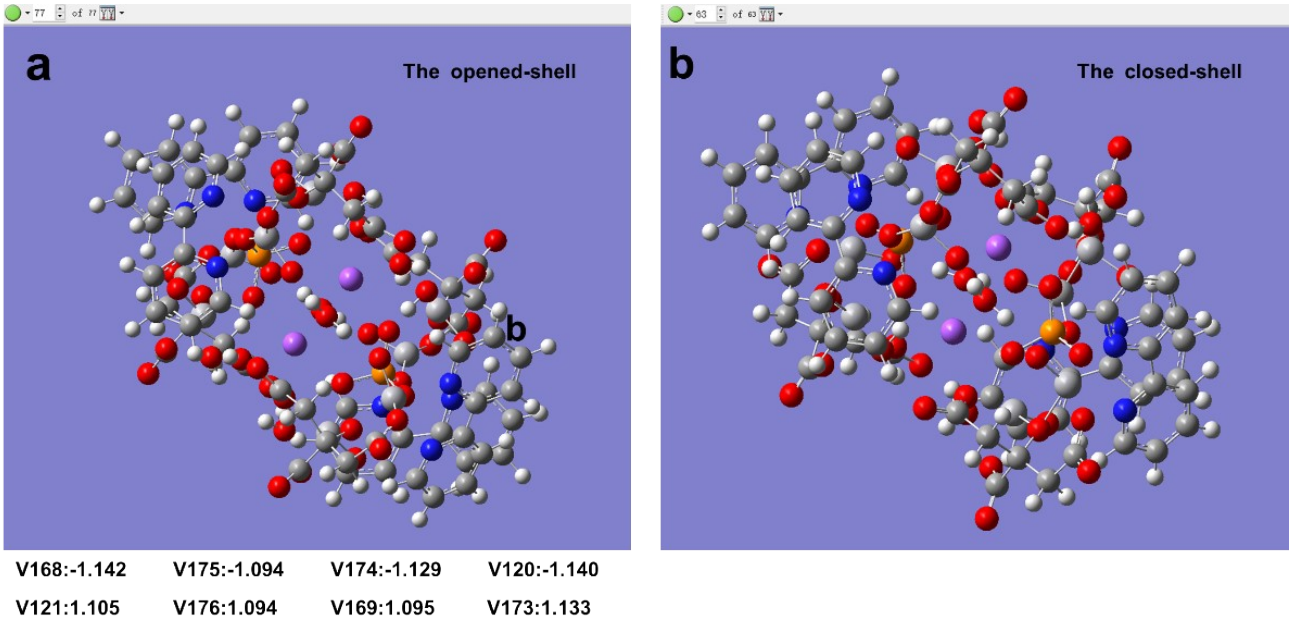

Fig. S18. Optimized structure diagram and the spin multiples of each vanadium atom of 9V-N and 6V-S

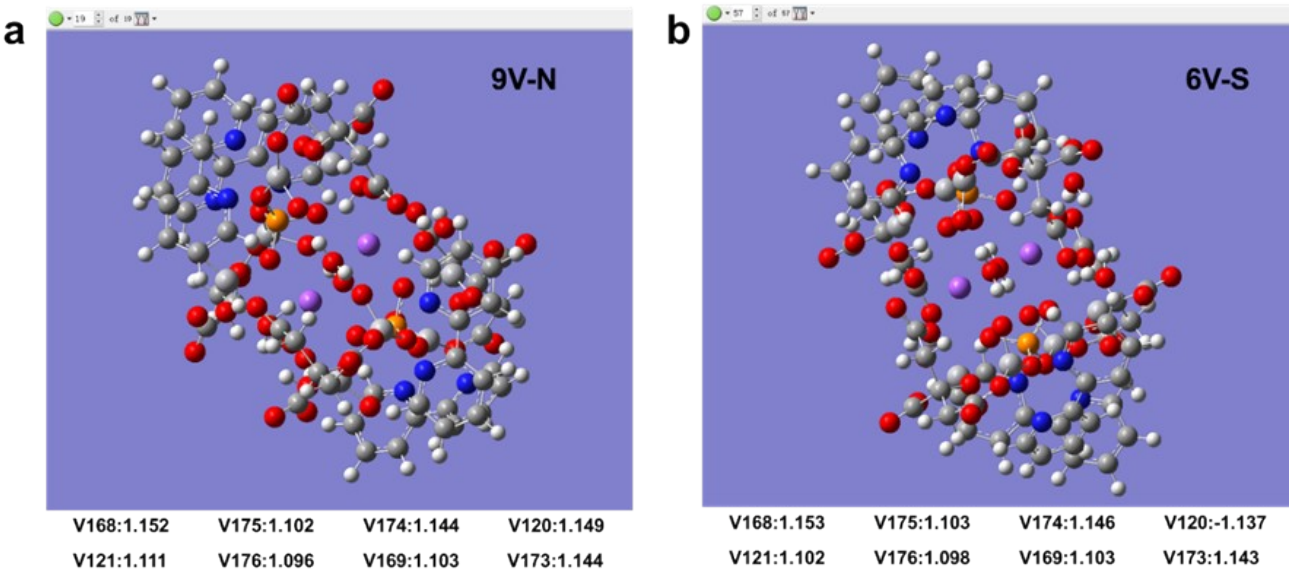

References

1. J. Du, Y.-Y. Ma, W.-J. Cui, S.-M. Zhang, Z.-G. Han, R.-H. Li, X.-Q. Han, W. Guan, Y.-H. Wang, Y.-Q. Li, Y. Liu, F.-Y. Yu, K.-Q. Wei, H.-Q. Tan, Z.-H. Kang and Y.-G. Li, Unraveling photocatalytic electron transfer mechanism in polyoxometalate-encapsulated metal-organic frameworks for high-efficient CO_2 reduction reaction, *Appl. Catal. B.*, 2022, **318**, 121812.
2. M. Lin, M. Luo, Y. Liu, J. Shen, J. Long and Z. Zhang, 1D S-scheme heterojunction of urchin-like SiC-$W_{18}O_{49}$ for enhancing photocatalytic CO_2 reduction, *Chinese J. Catal.*, 2023, **50**, 239-248.
3. I. Khan, S. Khan, S. Y. Wu, H. T. Chen, A. Zada, M. Haider, J. Khan, S. Ullah, S. P. Ju and S. Wang, Synergistic functionality of dopants and defects in Co-phthalocyanine/B-CN Z-Scheme photocatalysts for promoting photocatalytic CO_2 reduction reactions, *Small*, 2023, **19**, e2208179.
4. T. Su, M. Sun, J. Wu, L. Chen, H. Ji and Z. Qin, Black phosphorus/Bi_2MoO_6 Z-scheme heterojunction for enhanced photocatalytic CO_2 reduction, *J. Phys. D.*, 2023, **56**, 355503.
5. S. Li, Y. Yang, S. Wan, R. Wang, M. Yu, F. Song and Q. Zhong, Supramolecular self-assemble deficient carbon nitride nanotubes for efficient photocatalytic CO_2 reduction, *J. Colloid Interface Sci.*, 2023, **651**, 726-733.
6. P. N. Nguyen, T. T. Tran, Q. A. Thi Nguyen, Y. Kawazoe, S. V. P. Vattikuti, L. V. Le, V. Q. Bui, T. M. Nguyen and N. N. Dang, Constructing a rhenium complex supported on g-C_3N_4 for efficient visible-light-driven photoreduction of CO_2 to CO via a novel Z-scheme heterojunction, *J. Mater. Chem. A.*, 2023, **11**, 17145.
7. K. Zhang, Y. Xu, F. Liu, G.-P. Yan and S.-W. Guo, Preparation and properties of ZnS–CdSe@Co/N–C core/shell composites for visible light photoconversion of CO_2, *New J. Chem.*, 2023, **47**, 12550-12553.
8. Y. Benseghir, A. Solé-Daura, J. Marrot and L. Dalecky, Understanding the photocatalytic reduction of CO_2 with heterometallic molybdenum(V) phosphate polyoxometalates in aqueous media, *ACS Catal.*, 2021, **12**, 453-464.
9. S. L. Xie, J. Liu, S. L. Li, Y. Q. Lan and Z. M. Su, Hetero-metallic active sites coupled with strongly reductive polyoxometalate for selective photocatalytic CO_2-to-CH_4 conversion in water, *Chem. Sci.*, 2019, **10**, 185-190.
10. C. Ban, Y. Duan, Y. Wang, J. Ma, K. Wang, J. Meng, X. Liu, C. Wang, X. Han, G. Cao, L. Gan and X. Zhou, Isotype heterojunction-boosted CO_2 photoreduction to CO, *Nanomicro Lett.*, 2022, **14**, 74.
11. J. Jiao, Y. Wei, Y. Zhao, Z. Zhao, A. Duan, J. Liu, Y. Pang, J. Li, G. Jiang and Y. Wang, AuPd/3DOM-TiO_2 catalysts for photocatalytic reduction of CO_2 : High efficient separation of photogenerated charge carriers, *Appl. Catal. B.*, 2017, **209**, 228-239.
12. X. Shi, X. Dong, Y. He, P. Yan and F. Dong, Light-induced halogen defects as dynamic active sites for CO_2 photoreduction to CO with 100% selectivity, *Sci. Bull.*, 2022, **67**, 1137-1144.
13. L. Zhu, H. Li, Q. Xu, D. Xiong and P. Xia, High-efficient separation of photoinduced carriers on double Z-scheme heterojunction for superior photocatalytic CO_2 reduction, *J. Colloid Interface Sci.*, 2020, **564**, 303-312.

14. Q. Xu, Y. Jin, T. Sun, T. Zheng, P. Zhang, Y. Han, Y. Wang, T. Li, D. Qi, L. Xu, D. Wang and J. Jiang, Theoretical and experimental investigation of the coordination effect on photocatalytic CO_2 reduction efficiency of cobalt single atom catalyst, *Chem. Eng. J.*, 2023, **479**, 147837.
15. S. Xia, C. Wei, Y. Zhai, B. Ding, J. Yu and J. Yan, Ultrasonic cavitation enhanced photocatalytic CO_2 reduction by superior flexible black $BaTiO_3$ nanofibers, *Chem. Eng. J.*, 2023, **475**, 146516.
16. X.-Y. Zhang, P. Wang, X.-Y. Lu, Y. Zhang and W.-Y. Sun, Synergistic effect on photocatalytic CO_2 reduction of facet-engineered Fe-soc-MOFs with photo-deposited PtO species, *Chem. Eng. J.*, 2023, **476**, 146560.
17. G. Chen, X. Cheng, J. Zhang, Q. Wan, R. Duan, B. Han, J. Cui, J. Xiang, B. Guan, X. Xing, G. Mo and Z. Wu, Water nanodomains for efficient photocatalytic CO_2 reduction to CO, *Green Chem.*, 2021, **23**, 9078-9083.
18. Y. X. Pan, Y. You, S. Xin, Y. Li, G. Fu, Z. Cui, Y. L. Men, F. F. Cao, S. H. Yu and J. B. Goodenough, Photocatalytic CO_2 reduction by carbon-coated indium-oxide nanobelts, *J. Am. Chem. Soc.*, 2017, **139**, 4123-4129.
19. Z. H. Yan, B. Ma, S. R. Li, J. Liu, R. Chen, M. H. Du, S. Jin, G. L. Zhuang, L. S. Long, X. J. Kong and L. S. Zheng, Encapsulating a Ni(II) molecular catalyst in photoactive metal-organic framework for highly efficient photoreduction of CO_2, *Sci. Bull.*, 2019, **64**, 976-985.
20. P. Niu, Z. Pan, S. Wang and X. Wang, Tuning crystallinity and surface hydrophobicity of a cobalt phosphide cocatalyst to boost CO_2 photoreduction performance, *ChemSusChem*, 2021, **14**, 1302-1307.
21. X. Lin, Z. Xie, B. Su, M. Zheng, W. Dai, Y. Hou, Z. Ding, W. Lin, Y. Fang and S. Wang, Well-defined Co_9S_8 cages enable the separation of photoexcited charges to promote visible-light CO_2 reduction, *Nanoscale*, 2021, **13**, 18070-18076.
22. Y. Liu, J. Wang, P. Ma, J. Wang and J. Niu, Enhanced photoinduced baeyer–villiger oxidation of ketones by introducing trinuclear ruthenium clusters into polyoxometalate-based metal–organic frameworks, *Chem. Mater.*, 2023, **35**, 3941-3950.
23. M. J. Frisch, G. W. Trucks, H. B. Schlegel, G. E. Scuseria, M. A. Robb, J. R. Cheeseman, G. Scalmani, V. Barone, G. A. Petersson, H. L. Nakatsuji, X.; , M. Caricato, A. V. Marenich, J. Bloino, B. G. Janesko, R. Gomperts, B. Mennucci, H. P. Hratchian, J. V. Ortiz, A. F. Izmaylov, J. L. Sonnenberg, D. Williams-Young, F. Ding, F. Lipparini, F. Egidi, J. Goings, B. Peng, A. Petrone, T. Henderson, D. Ranasinghe, V. G. Zakrzewski, J. Gao, N. Rega, G. L. Zheng, M. W.; Hada, M. Ehara, K. Toyota, R. Fukuda, J. Hasegawa, M. Ishida, T. Nakajima, Y. Honda, O. Kitao, H. Nakai, T. Vreven, K. Throssell, J. A. Montgomery, J. Peralta, J. E.; , F. Ogliaro, M. J. Bearpark, J. J. Heyd, E. N. Brothers, K. N. Kudin, V. N. Staroverov, T. A. Keith, R. Kobayashi, J. Normand, K. Raghavachari, A. P. Rendell, J. C. Burant, S. S. Iyengar, J. Tomasi, M. Cossi, J. M. Millam, M. Klene, C. Adamo, R. Cammi, J. W. Ochterski, R. L. Martin, K. Morokuma, O. Farkas, J. B. Foresman and D. J. Fox, Gaussian 16, Revision C.01,; Gaussian, Inc.:Wallingford, CT, 2016.
24. A. D. Beck, Density-functional thermochemistry. III. The role of exact exchange., *J. Chem.Phys.*, 1993, **98**, 5648-5652.

25. W. Yang, Parr, R. G. & Lee, C., Development of the colle-salvetti correlation-energy formulainto a functional of the electron density., *Phys. Rev. B.*, 1988, **37**, 785-789.
26. S. Grimme, Antony, J., Ehrlich, S. & Krieg, H., A consistent and accurate ab initio parametrization of density functional dispersion correction (DFT-D) for the 94 elements HPu, *J. Chem. Phys.*, 2010, **132**, 154102.
27. A. V. Marenich, Cramer, C. J. & Truhlar, D. G, Universal solvation model based on solute electron density and on a continuum model of the solvent defined by the bulk dielectric constant and atomic surface tensions, *J. Phys. Chem. B.*, 2009, **113**, 6378-6396.
28. Y. T. Zhao, D. G, The M06 suite of density functionals for main group thermochemistry, thermochemical kinetics, noncovalent interactions, excited states, and transition elements: two new functionals and systematic testing of four M06-class functionals and 12 other functionals, *Theor. Chem. Acc.*, 2008, **120**, 215-241.